Supplementary information:
Direct observation of nanoscale pinning centers in quasi single-phase $Ce(Co_{0.8}Cu_{0.2})_{5.4}$ magnets

Nikita Polin[1], Shangbin Shen[2], Fernando Maccari[2], Alex Aubert[2], Esmaeil Adabifiroozjaei[3], Tatiana Smoliarova[5], Yangyiwei Yang[2], Xinren Chen[1], Yurii Skourski[6], Alaukik Saxena[1], András Kovács[7], Rafal E. Dunin-Borkowski[7], Michael Farle[5], Bai-Xiang Xu[2], Leopoldo Molina-Luna[3], Oliver Gutfleisch[2], Baptiste Gault[1,4], Konstantin Skokov[2]

[1] Max-Planck-Institut für Nachhaltige Materialien, 40237 Düsseldorf, Germany
[2] Institute of Materials Science, Technische Universität Darmstadt, 64287 Darmstadt, Germany
[3] Advanced Electron Microscopy Division, Institute of Materials Science, Department of Materials and Geosciences, Technische Universität Darmstadt, Peter-Grünberg-Str. 2, Darmstadt 64287, Germany
[4] Department of Materials, Royal School of Mines, Imperial College, Prince Consort Road, London SW7 2BP, United Kingdom
[5] Faculty of Physics and Center for Nanointegration (CENIDE), University Duisburg Essen, Duisburg 47057, Germany
[6] Dresden High Magnetic Field Laboratory (HLD-EMFL), Helmholtz-Zentrum Dresden-Rossendorf, Dresden 01328, Germany
[7] Ernst Ruska-Centre for Microscopy and Spectroscopy with Electrons, Forschungszentrum Jülich, Jülich 52425, Germany

A. Magnetic characterization

Magnetic parameters obtained from homogenized $R(Co,Cu)_5$ single-phase single-crystalline samples are generally accepted as the most representative values of K_u and M_s for a given chemical composition, and are therefore regarded as the intrinsic magnetic properties of the material at that composition [S1,S2]. In contrast, measurements of K_u, M_s, and, in particular, the exchange stiffness A, at nanometer-scale Cu-rich cell boundaries are currently not experimentally accessible. To the best of our knowledge, no experimental study has locally quantified the Cu-dependence of these parameters. Existing atomistic simulations provide only a qualitative indication that both K_u and M_s decrease with increasing Cu content and are strongly reduced at high Cu concentrations [S3], while a systematic determination of Cu-dependent micromagnetic parameters is still lacking.

From a micromagnetic modeling perspective, capturing the pinning strength induced by nanoscale Cu concentration profiles primarily requires parameters that phenomenologically represent the local energy landscape and yield domain-wall widths consistent with experimental observations. The use of homogenized single-phase values for $K_u(x_{\mathrm{Cu}})$ and $M_s(x_{\mathrm{Cu}})$ is therefore both viable and consistent with current experimental capabilities, whereas the exchange stiffness A is approximated via the experimentally determined Bloch wall width using $\ell_{\mathrm{dw}} = \pi\sqrt{A/K_u}$, which is also widely employed in the micromagnetic simulations [S4].

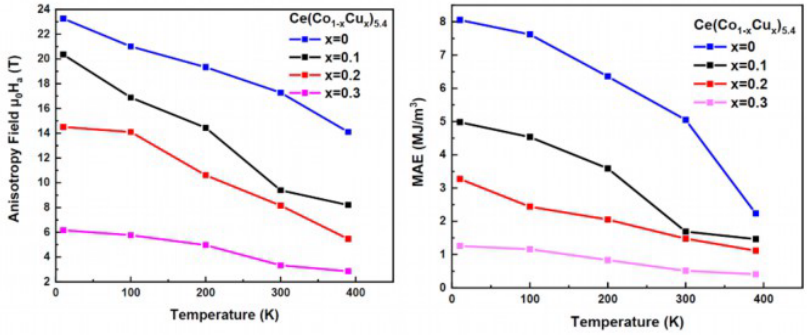

Figure S1 Intrinsic properties of the series of $Ce(Co_{1-x}Cu_x)_{5.4}$. The anisotropy field (left) and anisotropy energy (right) experimentally determined from homogenized nearly single-phase grains at different temperatures.

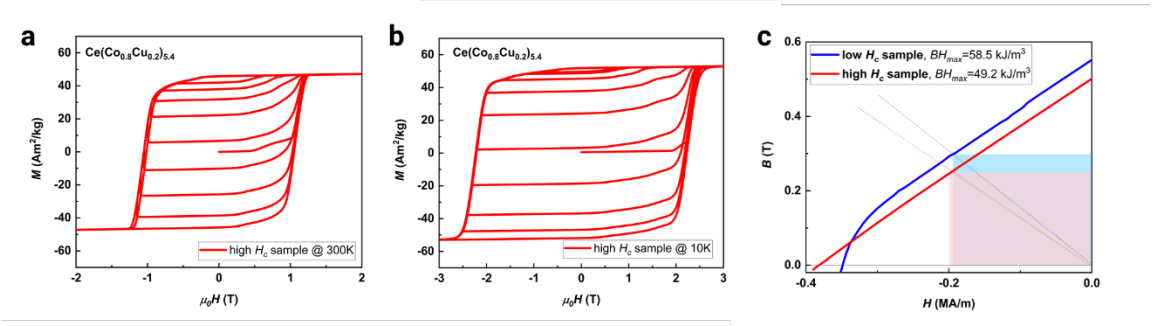

Figure S2a Magnetometry analysis: (a-b) partial hysteresis loops of the high H_c $Ce(Co_{0.8}Cu_{0.2})_{5.4}$ sample at 300K (a) and 10K (b). (c) second quadrant of the *B*-*H* hysteresis loop with BH_{max} indicated as rectangles. The maximum energy product BH_{max} for the low and high H_c samples are 58.5 kJ/m³ and 49.2 kJ/m³.

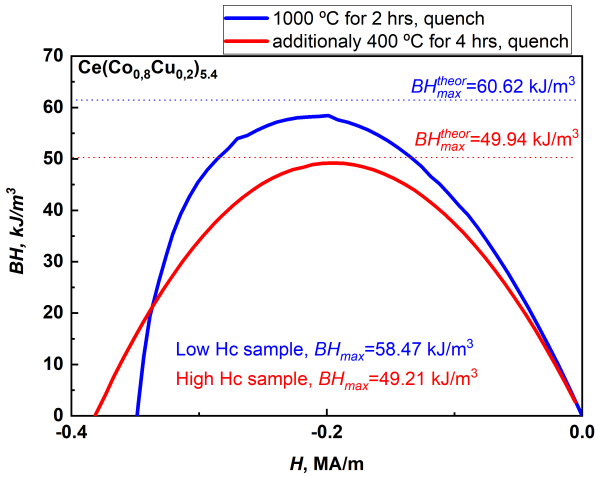

Figure S2b BH_{max} as a function of demagnetizing magnetic field. The experimental maximum energy product BH_{max} for the low and high H_c samples are 58.5 kJ/m³ and 49.2 kJ/m³, the theoretical maximum energy product BH_{max} calculated as $\frac{\mu_0 M_S^2}{4}$ for the low and high H_c samples are 60.62 kJ/m³ and 49.94 kJ/m³, that is very close to the experimental BH_{max} values.

We also performed an evaluation of $(BH)_{max}$ using the experimentally measured M_s value. The resulting theoretical $(BH)_{max} = \frac{\mu_0 M_S^2}{4}$ is very close to the experimentally observed value, indicating that the measured $(BH)_{max}$ is consistent with expectations from intrinsic magnetic properties.

B. Microstructure of polycrystalline samples

As Figure S3 shows, the microstructure of the high H_c sample is characterized by large grains of ~100-500μm (BSE image **Error! Reference source not found.**a) which have high degree of texture with misorientation angles between the grain are < 3° (EBSD, **Error! Reference**

source not found.b). The contrast in the BSE images stems from the slightly different orientation of the grains as it correlates with EBSD contrast. Note that this sample is randomly oriented as the EBSD color map shows.

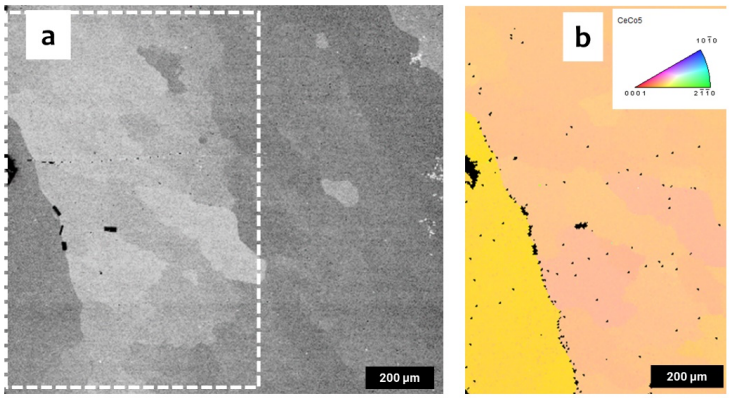

Figure S3 Microstructure characterization of $Ce(Co_{0.8}Cu_{0.2})_{5.4}$ high H_c polycrystalline sample by electron microscopy (a) in backscatter electron mode (BSE) and by (b) electron backscatter diffraction (EBSD). The sample possesses large grains ~100-500 µm in size and a high degree of texture

C. Atom probe tomography: specimen preparation and further analyses

Table S1 Compositions and standard deviations derived from APT measurements shown in **Error! Reference source not found.**. The calculations for Cu-rich and Cu-poor regions were executed as described in detail in Ref. [S5]. The standard deviations for the total compositions are calculated from different APT measurements of the same sample.

Sample	Region	Ce (at. %)	Co (at. %)	Cu (at. %)	Composition
High H_c sample	Cu-rich	15.77±0.18	63.62±0.37	20.61±0.32	$Ce(Co_{0.76}Cu_{0.24})_{5.34}$
	Cu-poor	16.80±0.22	74.98±0.46	8.22±0.26	$Ce(Co_{0.90}Cu_{0.10})_{4.95}$
	Total	16.19±0.17	69.47±0.69	14.35±0.15	$Ce(Co_{0.83}Cu_{0.17})_{5.18}$
Low H_c sample	Cu-rich	15.57±0.35	63.31±0.40	21.13±0.67	$Ce(Co_{0.75}Cu_{0.25})_{5.42}$
	Cu-poor	16.39±0.31	72.19±0.44	11.42±0.22	$Ce(Co_{0.86}Cu_{0.14})_{5.10}$
	Total	15.96±0.16	68.93±0.69	15.11±0.15	$Ce(Co_{0.82}Cu_{0.18})_{5.27}$

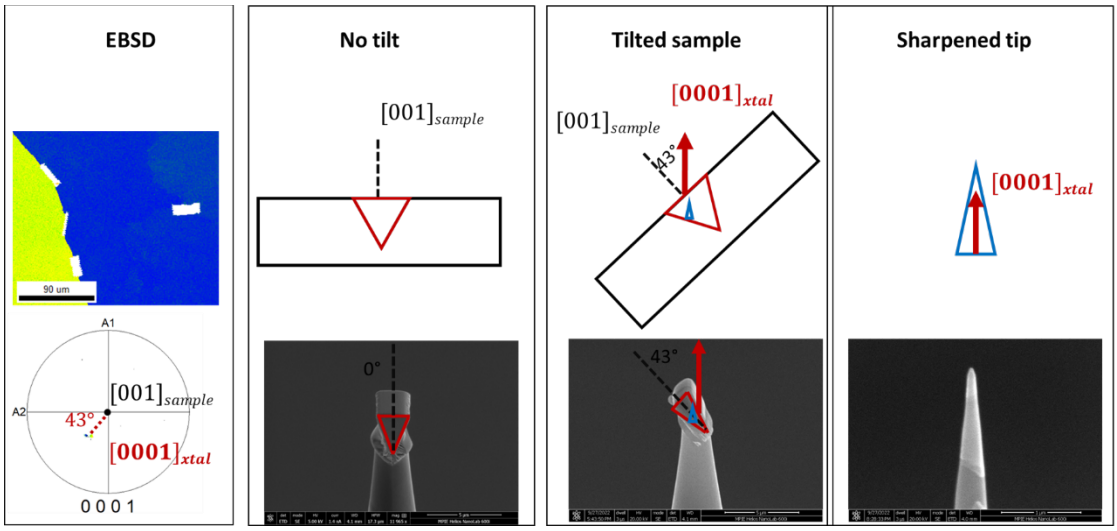

Figure S4 APT needle preparation by FIB with a desired orientation. First image: EBSD map (top) and pole figure (bottom), determining the grain orientation to the sample's normal. Second image: the conventional lift-out schematics (top) and corresponding SEM image of the APT specimen before sharpening (bottom). Third image: schematics of the lift-out under an appropriate angle, prior determined by EBSD to be 43° (top), and corresponding SEM image of the APT specimen before sharpening (bottom). Forth image: sharpened APT tip with correct orientation schematics (top) and corresponding SEM image of the APT specimen after sharpening. Red and blue triangles indicate the APT samples before and after sharpening, the sample normal direction $[001]_{sample}$ and the *c*-axis of the crystal $[0001]_{xtal}$ enclose an angle of 43°.

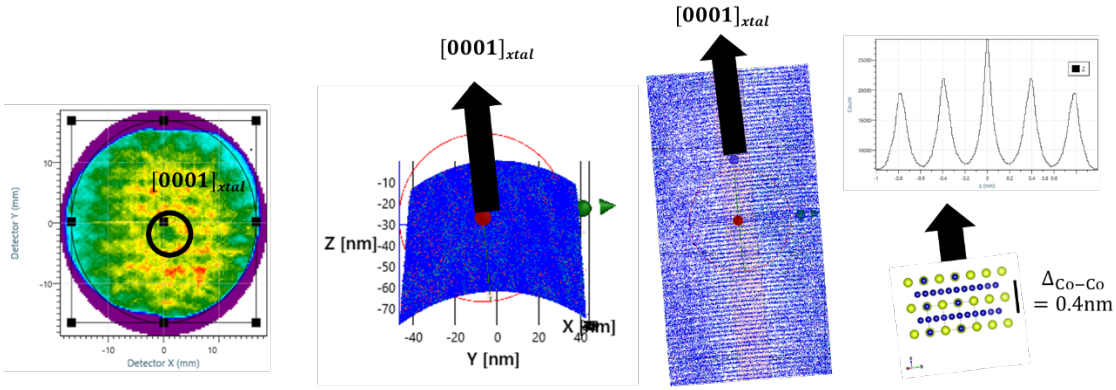

Figure S5 APT crystallographic analysis. First: identification of the [0001] pole in the detector histogram. Second: low magnification APT reconstruction. Third: high magnification in a slice of an APT reconstruction with visible atomic planes. Fourth: spatial distribution map (SDM, top) and structure model (bottom).

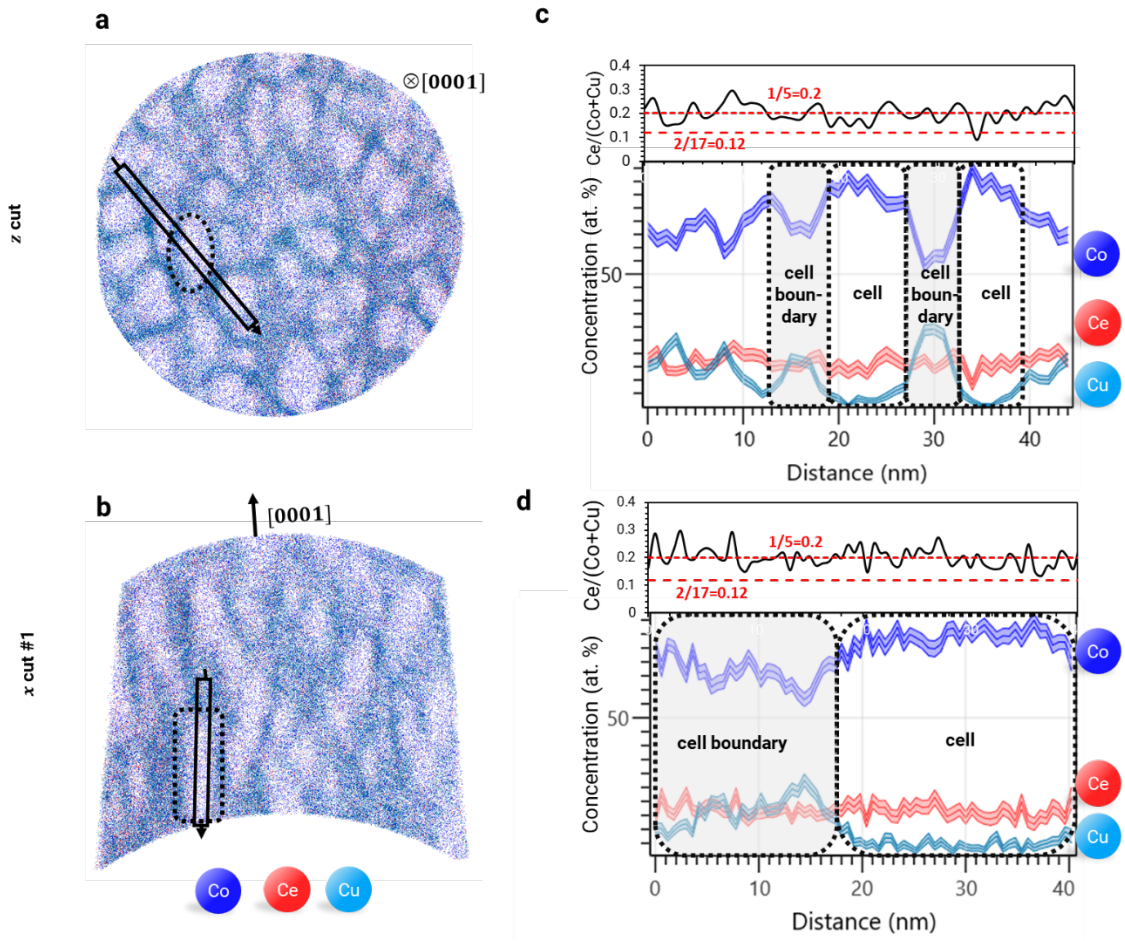

Figure S6 APT analysis of the cellular structure in the high H_c sample: (a,b) 3D reconstructions. (c,d) Additional 1D profiles and calculated rare earth/transition metals ratio Ce/(Co+Cu)..

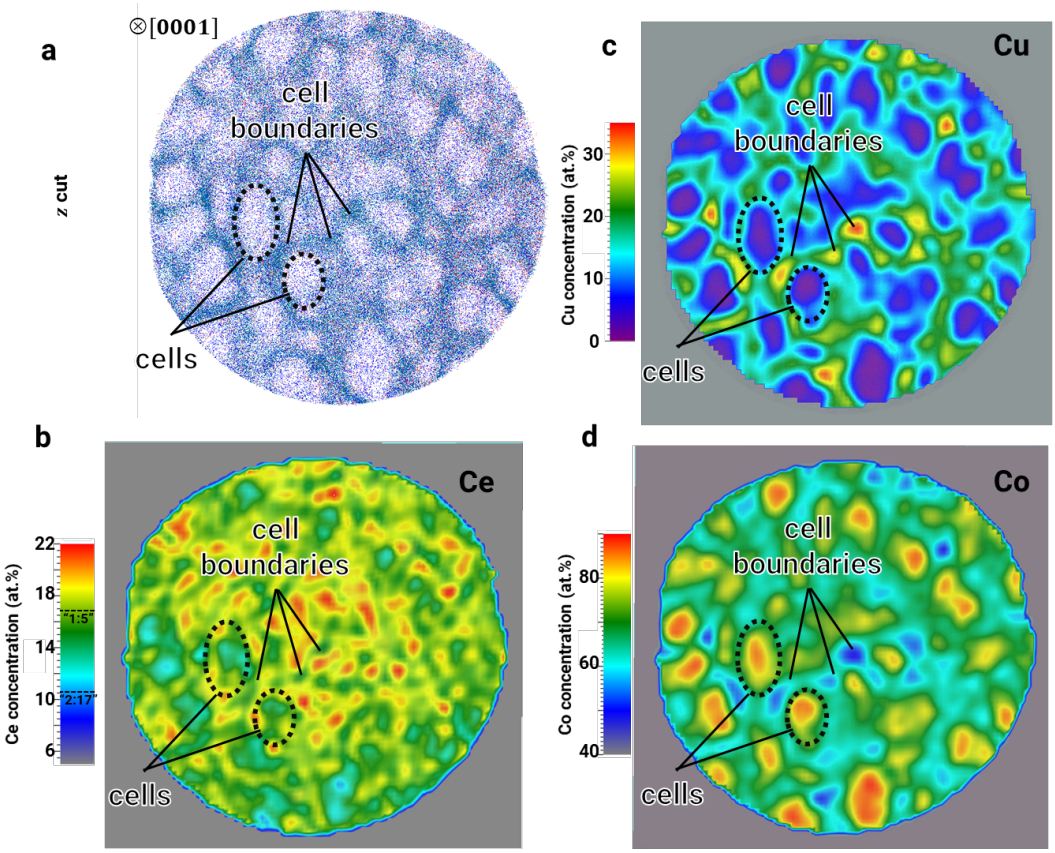

Figure S7 APT analysis of the cellular structure in the high H_c sample in cross section (z cut): (a) 10nm thin slice of APT data and corresponding 2D concentration maps of (b) Ce, (c) Cu and (d) Co. In the Ce colorbar, the Ce concentrations corresponding to the 1:5 (10.5 at.%) and 2:17 (16.7 at. %) phases are marked.

D. Transmission electron microscopy: further analyses

Unlike the single-grain samples used in the remainder of this study, the TEM analysis in **Figure S9** was performed on a polycrystalline high H_c sample to investigate grain boundary (GB) structure and chemistry.

In **Figure S9a-c**, bright-field STEM images with increasing magnification show a chemically homogeneous matrix, that is Cu-depleted relative to Cu-enriched grain boundaries (GBs), which contain ~100nm large Cu-rich precipitates, cf. EDX profile in **Figure S9d**. These GB features resemble those reported in Ta-containing $Ce(Co,Cu)_5$ single crystals with composition $Ce_{15.7}Ta_{0.6}Co_{67.8}Cu_{15.9}$, prepared by self-flux technique [52]. Based on low-magnification TEM image in **Figure S9**a, the precipitate volume fraction is roughly estimated be to <5%.

A detailed view of the GB precipitates in **Figure S9e** by STEM and corresponding energy-dispersive X-ray spectroscopy (EDX) chemical maps in **Figure S9f-h** reveal an increase in Cu, decrease of these GB precipitates. **Figure S9i** shows a high magnification BF TEM image of a representative precipitate with its associated fast Fourier transformed image (**Figure S9j**), displaying satellite peaks at $\frac{1}{2}\{110\}$. These features can be reproduced by simulations (**Figure S9l**), assuming an ordered arrangement of Cu atoms on Co sites along one of six

symmetry-equivalent [100] directions, as depicted in **Figure S9**. Crystallographic data for the $Ce(Co,Cu)_5$ with Cu-ordering is available in the supplementary information (see CIF file). Although the diffraction pattern also matches with Ce_2Co_{17} phase as suggested by Leamy et al. [21], the expected compositional contrast between the $CeCo_5$ and Ce_2Co_{17} phases is not observed in our data: EDX chemical map in **Figure S9h** and the EDX line profile in **Figure S9d** show no variation of Ce-content. This suggests, that no transition from 2:17 phase to 1:5 has occurred, in line with APT results from the matrix. Hence we conclude that in GB precipitates, higher Cu-concentration correlates to the presence of a Cu-ordered $CeCo_5$-phase.

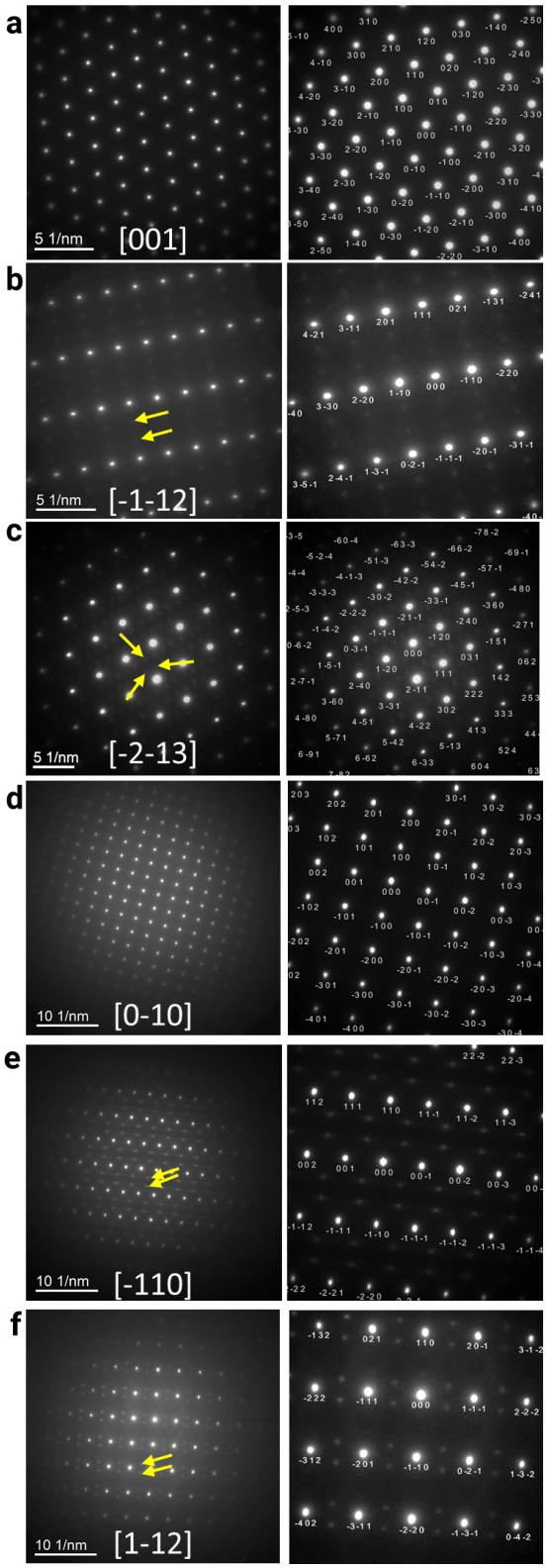

Figure S8 Series of diffraction images from the matrix of the CeCoCu high H_c sample with different zone axes indicated in the respective images, with unindexed pattern in the left row and indexed main reflection in the right row. The extra reflections (satellite peaks) are indicated with yellow arrow and are only observed in

higher index patters. Images (a-c) stem from a TEM specimen with c-axis out plane and (d-f) with c-axis in-plane. The satellite peaks are observed at orientations different from [001] (a) and [0-10] (d).

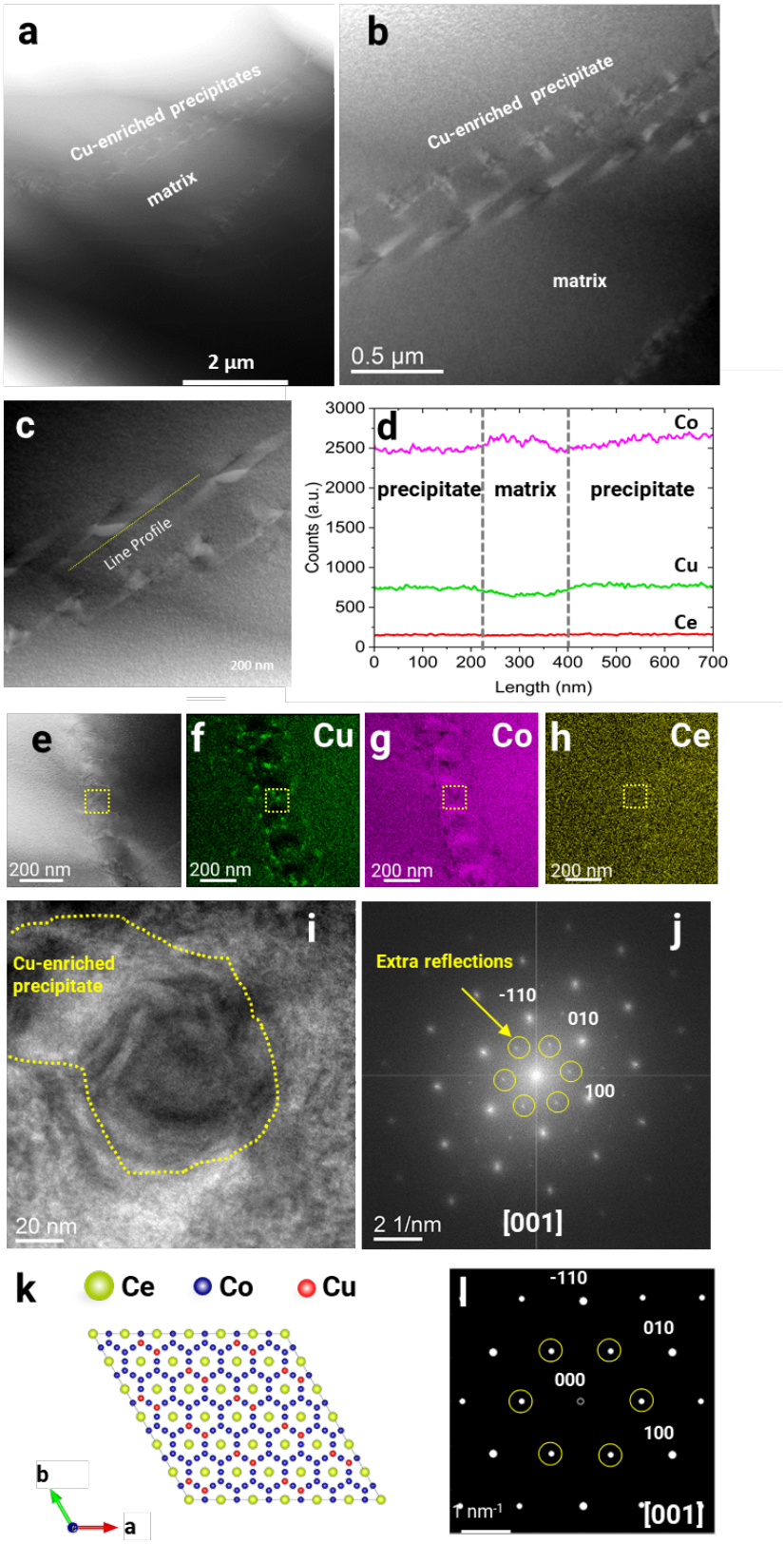

Figure S9 TEM analysis of a polycrystalline high H_c sample. (**a-c**) Bright-field STEM images with increasing magnification. (**d**) EDX profile across the line indicated in (c). (**e-h**) STEM image and corresponding energy-dispersive X-ray spectroscopy (EDX) chemical maps of Cu, Co and Ce. (**i**) BF-TEM image of a representative precipitate and (**j**) its associated fast Fourier transformed image. (**k**) Structural models with 3×3×1 cells of

$CeCo_5$ with Cu-ordering in lines on Co-cites. (**l**) Simulated diffraction along the [001] zone axis using the structural models in (k).

E. Mesoscale magnetic domain structure

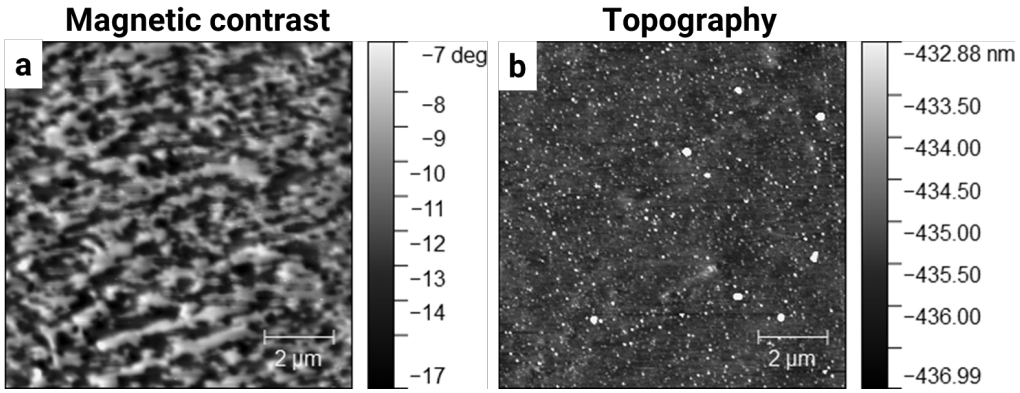

Figure S10 Magnetic domain structure characterization of the high H_c sample by MFM: (a) Magnetic contrast (b) Topography. The nominal *c*-axis is oriented out of plane.

F. Measuring the domain wall width

Measuring the domain wall width from the phase shift across a 180° domain wall is one of the most accurate TEM-based approaches. In our FIB-prepared lamella, the strong shape anisotropy confines the magnetization to the film plane, consistent with the in-plane magnetic easy axis of the material. This configuration favours a Néel-type domain wall, for which the in-plane magnetization rotation produces a phase signal to which magnetic imaging in TEM is most sensitive. Induction mapping further confirms that the magnetization rotates close to 180°, validating the use of the phase-shift profile for domain wall width determination.
However, for Cu-rich and Cu-poor regions the measurement was performed on an ~80 nm thick TEM specimen containing many such regions along the electron-beam path. Because the electron wave integrates the magnetic induction over the entire thickness, the extracted domain wall width reflects the collective magnetic properties of the $Ce(Co\text{-}Cu)_{5.4}$ system rather than isolated contributions from Cu-rich or Cu-poor regions. Moreover, the domain wall width is determined by the ratio of exchange stiffness (A) to magnetocrystalline anisotropy (K), both of which are effective parameters arising from the combined microstructural regions. Consequently, the material exhibits a single characteristic domain wall, and separate wall widths for Cu-rich and Cu-poor regions cannot be distinguished experimentally.

References:

S1. Lectard, E., Allibert, C. H. & Ballou, R. Saturation magnetization and anisotropy fields in the Sm(Co 1− x Cu x) 5 phases. *Journal of Applied Physics* **75**, 6277–6279 (1994).
S2. Liu, B., Wang, H., Xu, H., Liu, J. & Jiang, C. Atomic-Scale Transition Zones Determined Coercivity in Samarium-Cobalt Based Permanent Magnets. *Adv Funct Materials* **33**, 2304711 (2023).
S3. Choudhary, R., Palasyuk, A., Nlebedim, I. C., Ott, R. T. & Paudyal, D. Atomic cooperation in enhancing magnetism: (Fe, Cu)-doped CeCo5. *Journal of Alloys and Compounds* **839**, 155549 (2020).
S4. Kronmüller, H. & Goll, D. Micromagnetism of advanced hard magnetic materials. *International Journal of Materials Research* **100**, 640–651 (2009).
S5 T.N. Lamichhane, M.T. Onyszczak, O. Palasyuk, S. Sharikadze, T.H. Kim, Q. Lin, M.J. Kramer, R.W. McCallum, A.L. Wysocki, M.C. Nguyen, V.P. Antropov, T. Pandey, D. Parker, S.L. Bud'ko, P.C. Canfield, A. Palasyuk, Single-Crystal Permanent Magnets: Extraordinary Magnetic Behavior in the Ta -, Cu -, and Fe -Substituted CeCo5 Systems, Phys. Rev. Appl. 11 (2019) 1. https://doi.org/10.1103/PhysRevApplied.11.014052.